The composite nature of Dust-Obscured Galaxies (DOGs) at z∼2-3 in the COSMOS field: I. A Far-Infrared View

L. Riguccini[1,2*], E. Le Floc'h[3], J.R. Mullaney[4], K. Menéndez-Delmestre[1], H. Aussel[3], S. Berta[5], J. Calanog[6], P. Capak[7], A. Cooray[6], O. Ilbert[8], J. Kartaltepe[9], A. Koekemoer[10], D. Lutz[5], B. Magnelli[5], H. McCracken[11], S. Oliver[12], I. Roseboom[13], M. Salvato[14], D. Sanders[15], N. Scoville[16], Y. Taniguchi[17], E. Treister[18],

[1] *Observatório do Valongo, Universidade Federal do Rio de Janeiro, Ladeira do Pedro Antônio 43, Saúde, Rio de Janeiro, RJ 20080-090, Brazil (riguccini@astro.ufrj.br)*
[2] *CAPES/BJT Science Without Borders Postdoctoral Fellow, Brazil*
[3] *Laboratoire AIM, CEA/DSM-CNRS-Université Paris Diderot, IRFU/Service d'Astrophysique, Bât.709, CEA-Saclay, 91191 Gif-sur-Yvette Cedex, France*
[4] *Department of Physics and Astronomy, Hicks Building, University of Sheffield, S3 7RH, U.K.*
[5] *Max-Planck-Institut für extraterrestrische Physik, Postfach 1312, Giessenbachstrasse 1, 85741 Garching, Germany*
[6] *Center for Cosmology, Department of Physics and Astronomy, University of California, Irvine, CA 92697, USA*
[7] *Spitzer Science Center, 314-6 Caltech, Pasadena, CA 91125, USA*
[8] *Laboratoire d'Astrophysique de Marseille, BP 8, Traverse du Siphon, 13376 Marseille Cedex 12, France*
[9] *National Optical Astronomy Observatory, 950 N. Cherry Ave., Tucson, AZ, 85719, USA*
[10] *Space Telescope Science Institute, 3700 San Martin Drive, Baltimore, MD 21218, USA*
[11] *Institut d'Astrophysique de Paris, UMR7095 CNRS, Université Pierre et Marie Curie, 98 bis Boulevard Arago, 75014 Paris, France*
[12] *Astronomy Centre, Department of Physics & Astronomy, University of Sussex, Brighton BN1 9QH, UK*
[13] *Institute for Astronomy, University of Edinburgh, Royal Observatory, Blackford Hill, Edinburgh EH9 3HJ, UK*
[14] *Max-Planck-Institute für Plasma Physics, Boltzmann Strasse 2, Garching 85748, Germany*
[15] *Institute for Astronomy, 2680 Woodlawn Dr., University of Hawaii, Honolulu, HI 96822, USA*
[16] *California Institute of Technology, MC 105-24, 1200 East California Boulevard, Pasadena, CA 91125, USA*
[17] *Research Center for Space and Cosmic Evolution, Ehime University, Bunkyo-cho, Matsuyama 790-8577, Japan*
[18] *Universidad de Concepción, Departamento de Astronomía, Casilla 160-C, Concepción, Chile*

ABSTRACT

Dust-Obscured galaxies (DOGs) are bright 24μm-selected sources with extreme obscuration at optical wavelengths. They are typically characterized by a rising power-law continuum of hot dust ($T_D \sim 200$-1000 K) in the near-IR indicating that their mid-IR luminosity is dominated by an an active galactic nucleus (AGN). DOGs with a fainter $24\,\mu$m flux display a stellar bump in the near-IR and their mid-IR luminosity appears to be mainly powered by dusty star formation. Alternatively, it may be that the mid-IR emission arising from AGN activity is dominant but the torus is sufficiently opaque to make the near-IR emission from the AGN negligible with respect to the emission from the host component. In an effort to characterize the astrophysical nature of the processes responsible for the IR emission in DOGs, this paper exploits Herschel data (PACS + SPIRE) on a sample of 95 DOGs within the COSMOS field. We derive a wealth of far-IR properties (e.g., total IR luminosities; mid-to-far IR colors; dust temperatures and masses) based on SED fitting. Of particular interest are the 24 μm-bright DOGs ($F_{24\mu m} >$1mJy). They present bluer far-IR/mid-IR colors than the rest of the sample, unveiling the potential presence of an AGN. The AGN contribution to the total 8-1000μm flux increases as a function of the rest-frame 8μm-luminosity irrespective of the redshift. This confirms that faint DOGs ($L_{8\mu m} < 10^{12}$ $L_\odot$) are dominated by star-formation while brighter DOGs show a larger contribution from an AGN.

Key words: Galaxies: high-redshift - Infrared: galaxies - Cosmology: observations

1   INTRODUCTION

The unprecedented sensitivity and angular resolution of the *Spitzer* Space Telescope at infrared (IR) wavelengths led to the discovery of a new type of galaxy that is extremely faint in the optical ($\sim 22{<}\text{R}{<}27$), yet bright at mid-infrared wavelengths (Houck et al. 2005; Dey et al. 2008; Fiore et al. 2008). These sources, known to as "Dust Obscured Galaxies" (hereafter, DOGs) in reference to the cause of their faintness at optical wavelengths, have extremely red optical-to-IR colors ($f_\nu(24\mu m)/f_\nu(R) > 982$). The incidence of DOGs is relatively low: only 8 % of 24 μm detected sources are DOGs, while $\sim$40 % of the sources in the 2 deg^2 COSMOS field optical catalog have similar R-band magnitude [22.4-26.4]. However, their contribution to the total IR output of the Universe at $z \sim 2$ where their source numbers peak is estimated to be at least 30% (Riguccini et al. 2011). This contribution increases to 50 % when considering the high-luminosity tail of their distribution at these redshifts (i.e., $L_{\rm IR} > 10^{12}$ L$_\odot$; e.g., Riguccini et al. 2011). DOGs have *IR* luminosities $> 10^{11}$ L$_\odot$ placing them in the LIRG and ULIRG[1] class of galaxies (e.g., Dey et al. 2008; Bussmann et al. 2009; Riguccini et al. 2011). Such luminosities require significant amounts of dust-heating, most probably arising from star-formation and/or high levels of nuclear activity (i.e., active galactic nucleus or AGN). A number of recent studies have split the DOG population along these lines: i.e., DOGs showing a "bump" at 1.6 μm indicative of star-formation (Farrah et al. 2008; Desai et al. 2009, hereafter bump DOGs) and DOGs displaying a rising power-law SED in the near- to mid-IR bands, suggesting a dominant AGN (Houck et al. 2005; Weedman et al. 2006, hereafter PL-DOGs). Estimating the star-formation rate of the latter has proved extremely difficult due to the dominant AGN component washing out any host galaxy signatures.

The faintness of DOGs at optical wavelengths has made the characterization of their physical properties particularly challenging. The launch of *the Herschel Space Telescope* in 2009 provided a new window onto these galaxies that is largely independent of dust obscuration, thereby giving us the clearest view yet of these galaxies. The wavelengths probed by *Herschel* cover the peak of the spectral energy distribution (hereafter, SED) of DOGs at the redshifts where their numbers are highest (i.e., $1.5 \lesssim z \lesssim 3$). This allows us to accurately constrain important properties, including the total IR luminosity as well as dust temperature and mass. The aim of this work is to use the combined diagnostic powers of both *Spitzer* and *Herschel* observations to determine how these properties relate to the dominant source of energy in these galaxies be it AGN, intense star formation or a combination of both. For this we use a sample of Spitzer/MIPS 24 μm-selected DOGs (satisfying $F_{24\mu m} > 0.08$ mJy) selected from the COSMOS field (Scoville et al. 2007), and detected in all 5 *Herschel* bands. We calculate the contribution from AGN and/or star-formation to the total energy output of these galaxies via SED fitting and relate this to their dust temperature and masses.

The paper is organized as follows. Our data are de-

scribed in Sect. 2, the far- to mid-IR colors of DOGs sources are detailed in Sect. 3. The SED-fitting procedure used and the results obtained are described in Sect. 4. In Sect. 5 we present the model and results on the dust temperature and mass of our DOG sample and discuss if the presence of AGN signatures induce a particular trend in the T$_{dust}$ distribution. We discuss our results and present our conclusions in Sect. 6. Throughout this paper we assume a ΛCDM cosmology with H$_0$=70 km s^{-1}, $\Omega_m = 0.3$, and $\Omega_\Lambda = 0.7$. Unless otherwise specified, magnitudes are given in the AB system.

2   DATA

The sample of DOG sources is selected from the deep *Spitzer*/MIPS observations of the 2 deg^2 COSMOS field (Sanders et al. 2007). Our starting point are the 24 μm detected sources from the catalogue described in Le Floc'h et al. (2009) (see also Riguccini et al. 2011). We note that other studies further require a source to satisfy $f_{24\mu m} > 300$ mJy in order to classify it as a DOG (e.g., Dey et al. 2008). In this study we consider all sources satisfying $f_\nu(24\mu m)/f_\nu(R) > 982$ as DOGs. Furthermore, DOG studies focussing on heavily-obscured AGNs (e.g., Fiore et al. 2008, 2009; Treister et al. 2009) also impose an additional R-K$>$4.5 (vega) cut.

2.1   COSMOS observations

COSMOS is a wide-area equatorial field with deep coverage at all wavelengths spanning radio to X-rays (Hasinger et al. 2007; Schinnerer et al. 2007; Elvis et al. 2009). Crucial for this study is the deep IR coverage of this field, particularly at mid- to far-IR wavelengths by the *Spitzer Space Telescope* with the MIPS instrument (Le Floc'h et al. 2009) and, more recently, with PACS (Poglitsch et al. 2010) and SPIRE (Griffin et al. 2010) onboard *Hershel* (Pilbratt et al. 2010).

The extensive UV to near-IR coverage of COSMOS (e.g., Taniguchi et al. 2007; Capak et al. 2007) allows for precise photometric redshifts (hereafter, photo-z) to be derived for extragalactic sources within this field. For the photo-zs used in this work, we use an updated[2] version of the photometric redshift catalog of Ilbert et al. (2009) that provides photo-zs for 1 400 237 i$^+$-detected sources among the 2 017 800 sources of the COSMOS photometric catalog. These redshifts are obtained with an unprecedented accuracy, with a dispersion of $\sigma_{\Delta z/(1+z)} = 0.012$ for sources satisfying i^+_{AB} <24 and z<1.25. More relevant to this study − where we focus on dusty 24μm-selected sources that are very faint at optical wavelengths − is their comparison with the optically-faint spectroscopic sample from the z-COSMOS survey (Lilly et al. 2007) where Ilbert et al. (2009) report a dispersion of only $\sigma_{\Delta z/(1+z)} = 0.06$ for sources with $23 < i^+_{AB} < 25$ at $1.5 < z < 3$. Given their accuracy for faint sources, we use these photo-zs for our 24 μm sources, matching their optical counterparts following the procedure outlined in Le Floc'h et al. (2009) and Riguccini et al. (2011).

---

[1] Luminous Infra-red Galaxies with $10^{11} L_\odot <$L$_{IR} < 10^{12}$ L$_\odot$ and Ultra-Luminous Infra-red Galaxies with L$_{IR} > 10^{12}$ L$_\odot$ (e.g., Sanders et al. 1988a,b)

[2] version 1.8: the main improvements compared to Ilbert et al. (2009) reside in relying on the median of the PDF to define the "best" photo-z, instead of the minimum χ^2

We briefly describe this approach in the following subsection.

2.2 The far-IR counterparts of 24 μm-selected sources

Our 24 μm parent sample (from Le Floc'h et al. (2009) and Riguccini et al. (2011)) contains 29 395 sources detected at 24 μm with $F_{24\mu m} >$ 80 μJy over a total area of 1.68 deg^2, which excludes regions contaminated by bright, saturated objects. In the interest of focussing on the sources' star-formation histories, we exclude X-ray detected AGNs down to a flux limit of $S_{0.5-2\,kev} = 5 \times 10^{-16}$ erg cm^{-2} s^{-1} based on AGN catalogs from Brusa et al. (2007, 2010) and Salvato et al. (2009).

We limit our counterpart identification to 24 μm sources with a 3-σ *PACS* detection at 100 μm and 160 μm. SPIRE fluxes will be used for a subset of our sample. The COSMOS field was observed as part of the PACS Evolutionary Probe (PEP, Lutz et al. 2011) and the Herschel Multi-tiered Extragalactic Survey (HerMES, Oliver et al. 2012) campaigns (i.e., PACS 100 & 160 μm and SPIRE 250, 350 & 500 μm respectively). The catalogs provided by PEP and HerMES calculate source fluxes in each of these 5 bands by performing PSF fitting at the positions of the 24 μm-detected sources from Le Floc'h et al. (2009). One of the key benefits of using such 24 μm "priors" as opposed to generating blind catalogues, is that it helps with deblending, which is particularly problematic at the longer *Herschel* wavelengths. The HerMES catalog was built following the method presented in Roseboom et al. (2010), based on the 24 μm position priors from Le Floc'h et al. (2009). The PEP catalog was obtained using the same *24 μm priors* (Berta et al. 2011). The reliability and the completeness of the PACS and SPIRE COSMOS catalogs are detailed in Lutz et al. (2011) and Oliver et al. (2012), respectively. We identify a total of 6 029 24 μm-detected sources with a >3-σ detection in the PACS-bands with $F_{100\mu m} >$ 3.1 mJy and $F_{160\mu m} >$ 6.3 mJy (see Table 1). We match these to the catalogue of optical sources from Ilbert et al. (2009) in order to obtain their photometric redshifts.

Given the much higher density of sources detected at optical wavelengths in COSMOS (Capak et al. 2007) compared to those detected with MIPS, a direct cross-correlation between the 24μm-selected catalog and the optical observations could lead to a large number of spurious associations with optically-detected galaxies randomly-aligned close to the line of sight of the MIPS sources. To minimize this, we first matched our 24μm catalogue to the K-band catalogue of McCracken et al. (2010), employing a matching radius of 2" and following the same procedure described in Le Floc'h et al. (2009) and Riguccini et al. (2011). Of the 6 029 sources in our sample, 5858 were found to have a K-band counterpart. In an attempt to reduce the number of non-matches, we also matched our 24μm catalogue to the IRAC-3.6 μm catalog from Capak et al. (2007), adopting the same 2" matching radius. This led to 34 additional matches, increasing to 5892 the number of MIPS-24 μm+Herschel sources with either a K-band or an IRAC-3.6 μm counterpart. These 5892 sources were then matched to the updated version of the i$^+$-band selected catalog of photometric redshifts from Ilbert et al. (2009) using a matching radius of
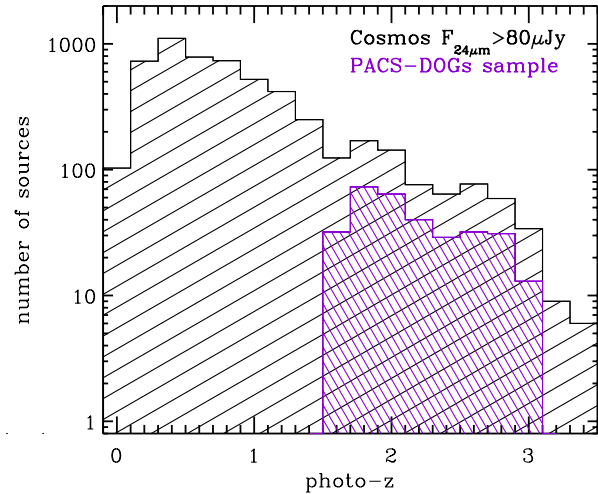

Figure 1. Photometric redshift distribution of the 24μm sources from Le Floc'h et al. (2009) in black and of the PACS-DOGs from this work in purple.

1". Of the 5892 sources, 5768 had i$^+$-band counterparts and associated photometric redshifts, leaving 261 sources among the 6 029 24 μm+Herschel sources (i.e., $\approx$ 4%) without photometric redshifts. These sources were excluded from any further analyses.

2.3 The PACS-DOGs sample

Our DOGs sample was selected from the 5 892 sources selected at 24 μm with a 3-σ detection in at least one of the PACS bands (100 or 160 μm). The DOGs criterion introduced by Dey et al. (2008) is based on the following: $F_{24\mu m}/F_R >982$ and $F_{24\mu m} >300$ μJy, where the latter is a direct consequence of the depth of the MIPS imaging in the Bootes field. Considering that the source-extraction performed by Le Floc'h et al. (2009) reaches a completeness of $\sim$90% with $F_{24\mu m} >80$ μJy, we extend the DOGs 24 μm-flux cut down to 80 μJy. The R-band magnitudes used in this work are from Ilbert et al. (2009) based on observations with the Subaru telescope by Capak et al. (2007); these include a correction for Galactic extinction – not applied in Capak et al. (2007) – and reach a limiting magnitude of $M_R >17.5$[3].

The sample contains 57 and 138 DOGs detected in only one of the PACS bands at 100 μm and 160 μm, respectively, while 119 DOGs are detected in both PACS bands. This amounts to a total of 314 PACS-detected DOG sources (cf Table 1) with $M_R >23.4$, $F_{100\mu m} >3.4$ mJy and $F_{160\mu m} >7.8$ mJy within the redshift range $1.5< z <3$ (see Fig. 1), where the DOGs criterion is the most efficient (e.g., Dey et al. 2008; Bussmann et al. 2009, 2012; Riguccini et al. 2011). We will use this sample in Sec. 3.
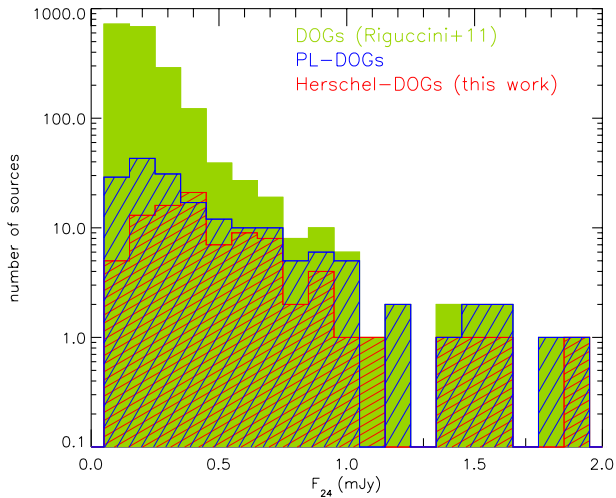
Figure 2. Distribution of 24 μm flux for the DOG parent sample ($\sim$2100 sources) from Riguccini et al. (2011) (green), PL-DOGs (blue) and the *Herschel*-DOGs from this work (red). The *Herschel*-DOGs distribution peaks at higher 24 μm fluxes ($\sim$0.36 mJy according to a Gaussian fit), compared to that of the whole DOGs sample ($\sim$0.14 mJy). The distribution of the PL-DOGs selected from Riguccini et al. (2011) also peaks slightly higher ($\sim$0.22 mJy) than the whole DOGs population distribution and is also more inclined to select 24 μm bright sources. See Sect. 2.4 for details.

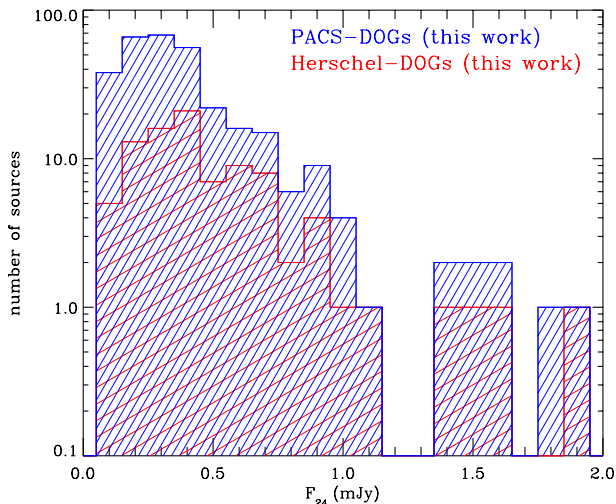**Figure 3.** Distribution of 24 μm flux of DOGs detected in at least one PACS-band (314 sources) in blue and the same *Herschel*-DOGs distribution than in Fig. 2 in red.

2.4   The *Herschel*-DOGs sample

Considering that we seek to undertake SED-fitting across the mid- to far-IR wavelength range, we further define a sub-sample of PACS-DOGs detected in all 5 Herschel bands ; this allows for a better constraint on the peak of the DOGs' SEDs. To achieve this we matched the PACS-DOGs sample

[3] We note that 24 μm-selected sources with no R-band detection are also considered DOG sources.

with the SPIRE catalog (Roseboom et al. 2010). This results in 95 Herschel-detected DOGs[4], i.e. detected in the 5 *Herschel* bands (see Table 1).

The fluxes in the PACS bands are obtained for all sources with a > 3-σ detection. Although the SPIRE catalog reaches a 3-σ limit of $\sim$ 10 mJy, $\sim$ 12 mJy and $\sim$ 15 mJy at 250, 350 and 500 μm respectively, the corresponding 3-σ extragalactic confusion limits are 14.4 mJy, 16.5 mJy and 18.3 mJy (Nguyen et al. 2010). In the SED-fitting procedure we are cautious (Magnelli et al. 2012a) when including fluxes that are lower than the 3-σ extragalactic confusion limits and use them merely as upper limits.

Among our sample of 95 Herschel-detected DOGs, 40 have their fluxes above the 3-σ threshold only for the 250 and 350 μm bands, 20 merely for the 250μm band, one DOG for the 350 and 500 μm bands and another DOG solely for the 350 μm; 9 of the Herschel-detected DOGs have all SPIRE fluxes below the 3-σ threshold. We quote upper limits for all of these cases. Only 24 sources have fluxes above the 3-σ limit in the three SPIRE bands.

We acknowledge that imposing a detection in the 5 *Herschel* bands will impart a bias towards the brightest and reddest IR sources in our sample. This is shown in Fig. 2, where the distribution of *Herschel*-DOGs peaks at higher 24 μm fluxes than that of the DOGs parent sample from Riguccini et al. (2011). Of particular interest is to note that although the faintest DOGs ($F_{24\mu m}$ <0.4 mJy) are missed by the *Herschel*-selection, beyond $F_{24\mu m}$ >0.4 mJy the Herschel-DOGs distribution is very similar to that of the DOG parent population (see Fig. 2). On the other hand, PL-DOGs – known to be mainly AGN dominated (e.g., Bussmann et al. 2009) – present a significantly stronger bias towards 24μm-bright sources: not only they have a 24μm flux distribution that peaks slightly higher than the whole DOGs population distribution, but their selection represents 60% of the DOG population with $F_{24\mu m}$ >1 mJy, compared to merely a 10% at $F_{24\mu m}$ =0.3 mJy Bussmann et al. (2009).

In this paper, two samples of DOGs are used. To study the IR colors of DOGs (Section 3) we use only PACS data and thus base our analysis on the 314 PACS-DOGs, in an effort to improve our statistics. For the remainder of our study we restrict our analysis to the 95 Herschel-detected DOGs, noting that both samples probe the same DOG population, as illustrated by their 24 μm flux distributions on Fig. 3. We focus our study on the differences observed between mid-IR bright DOGs ($F_{24\mu m} > 1$ mJy) and DOGs with more moderate fluxes ($\sim$ 0.2 mJy$<F_{24\mu m} < 1$ mJy).

2.5   The reliability of the photometric redshifts for the DOGs sample

The high accuracy of the photometric redshifts for sources of the COSMOS catalogue (see Sect. 2.1) make them highly reliable for statistical studies on large (i.e., >2 000) samples (e.g., Riguccini et al. 2011). However, because in this study we focus on significantly smaller numbers, we require particularly robust redshift measurements for each source. To ensure this, we checked the distribution of the probability density function (PDF) of the photometric redshift for

[4] All 95 Herschel-detected have R-band detections

Table 1. Number of sources

6 029	24 μm-sources with a 3-σ PACS detection (at 100 μm and 160 μm)
5 892	sources from the previous sample with a photo-z
314	DOGs (i.e., $F_{24\mu m}/F_R$ >982) with $F_{24\mu m}$ >80μJy and 1.5< z <3 and with a 3-σ detection in one or the two PACS-bands. Sample used for the far-IR/mid-IR color analysis [Sect. 3]
95	DOGs with $F_{24\mu m}$ >80μJy and 1.5< z <3 and with a 3-σ detection in the 2 PACS bands and with a detection (potentially > 3 σ) in the 3 SPIRE bands. Sample used for the remainder of the paper

each source and divided our sample into three categories, according to the photometric-redshift reliability. The categories are the following: (1) sources have a single, secure photo-z, for which the PDF has a gaussian shape with a single peak (39 sources); (2) those with multiple potential photo-zs, for which either the PDF's peak is spread over a wider range of redshifts ($\Delta z \sim 0.2$) or it includes a lesser peak which may correspond to another photometric redshift (24 sources); (3) those flagged as presenting inaccurate photo-zs, because their PDF shows clear multiple peaks of similar strength (32 sources). For sources in the last two categories, the photo-z is set to the highest peak value of the z-distribution and in the case of multiple peaks we keep the value of the subsequent peaks as secondary options. To get the most reliable and accurate fit to the SEDs of our sources, we use all of these potential photo-z values. We make a special note that six DOGs in our sample have a confirmed COSMOS spectroscopic redshift as part of the Fiber Multi Object Spectrograph (FMOS) spectroscopic redshift catalog (Kartaltepe et al., in prep.) which we use in our analysis for higher accuracy.

3 RESULTS: FAR-IR/MID-IR COLORS OF EXTREMELY MID-IR BRIGHT DOG SOURCES

The DOG sources are not only an extreme sub-sample of ULIRGs but also represent a mix between sources dominated by star-formation and those dominated by AGN activity (e.g., Houck et al. 2005; Fiore et al. 2008, 2009; Bussmann et al. 2009; Melbourne et al. 2012). In this paper we seek to quantify the AGN contribution of these sources and study the evolution of this contribution with respect to other galaxy properties, including redshift, the 8 μm rest-frame luminosity, total IR luminosity, dust temperature and dust mass.

Studies in the past years have explored the PL- and bump-DOGs population (e.g., Pope et al. 2008; Melbourne et al. 2009). It has been well established that PL-DOGs have an AGN contribution to their near-IR emission and that their far-IR emission is most likely dominated by star formation(Calanog et al. 2013). In this paper we aim to gauge the AGN contribution of these DOGs using *Herschel* far-IR data.

As an initial, crude assessment of the dominant process responsible for producing most of the IR output in DOGs (i.e., AGN vs. star formation), we first consider the far- to mid-IR colors (hereafter FIR/MIR) of our sample (e.g., Mullaney et al. 2012). Fig. 4 shows the 100 μm/24 μm and 160 μm/24 μm color distributions for our sample of PACS-detected DOGs as a function of redshift; we include all 24 μm -detected COSMOS sources for comparison. We see no noticeable trend for the DOGs sample at z$\geqslant$2; the curves shown for the 100/24 and 160/24 median color evolution with redshift seem to follow the same evolution than that of the whole 24 μm-detected sample. However, at lower redshifts the DOGs display a steeper evolution, with bluer 100/24 colors than the non-DOG 24μm-detected sources.

We find that the FIR/MIR distribution of both the bulk of the 24 μm comparison sample as well as the majority of our DOGs are well represented by the star forming templates from (Chary & Elbaz 2001, hereafter CE01) with IR luminosities $L_{IR} = 10^{12-12.5}$ L$_\odot$. This is to be expected given that IR-selected galaxies at z>1 tend to be of the LIRG or ULIRG class (e.g, Le Floc'h et al. 2005; Magnelli et al. 2009). We emphasize that although recent work has shown that CE01 local ULIRG SEDs are not good fits to z∼2 star-forming galaxies with similar IR luminosities (e.g., Elbaz et al. 2010, 2011; Nordon et al. 2010, 2012), the CE01 ULIRGs templates are good fits to our DOGs; 17 of our sources are fit using these templates with a χ^2 <5 (Sec. 4).

We consider the particular case of the brightest DOGs in our sample (i.e., $F_{24\mu m}$ >1 mJy) and find that they show a particular behavior in their FIR/MIR colors as a function of redshift: the brightest DOGs in our sample show significantly bluer PACS/24 μm colors than the general 24 μm-detected population (i.e, with $F_{24\mu m}$ >80 μJy). We discard the possibility that a variation in the Photodissociation regions (PDR) component and/or variation in the intensity of the field is responsible for the bluer color of these bright DOGs, by comparing to the 100 μm/24 μm colors derived from the templates of Magdis et al. (2012) (see Fig. 4). These SED templates are based on stacked ensembles at different redshift intervals, considering the varying radiation field and PDR contribution to ULIRGs as a function of redshift; for our study we rely on their starburst-dominated templates at the two relevant redshift intervals: $1.75 < z < 2.25$ and $2.27 < z < 3.0$. We compare to the FIR/MIR colors of AGN/galaxy composites – using the intrinsic AGN SED of Mullaney et al. (2011) and assuming different AGN contributions (25, 50, 100%) at 100 μm and 160 μm – and find significant similarities, suggesting that the brightest DOGs have a significant AGN contribution. As we consider higher redshifts, the median FIR/MIR color of these bright DOGs point towards a lower fraction of the AGN contribution, consistent with the SFRs of galaxies of similar mass increasing with redshift (e.g., Brinchmann et al. 2004; Daddi et al. 2007; Pannella et al. 2009; Magdis et al. 2010). We check the validity of these trends in the following section by looking at the AGN contribution (based on SED-fitting) as a function of the 24 μm flux.
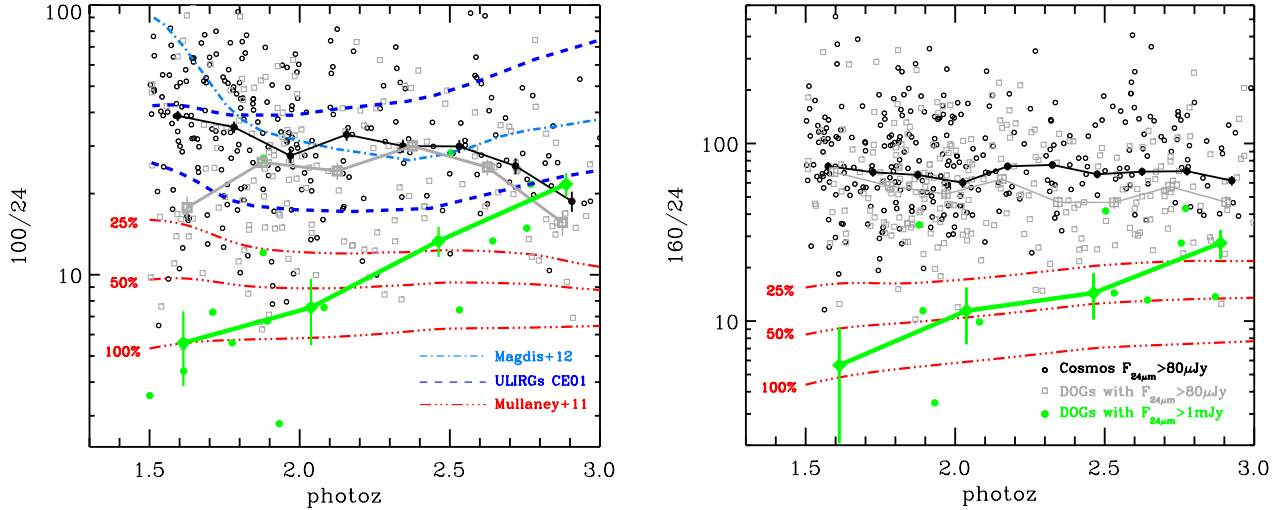
Figure 4. *Left:* Distribution of $100\mu m/24\mu m$ color as a function of redshift for all the 24 μm-selected sources detected at 100 μm (black open circles), the 176 DOGs detected at 100 μm with $F_{24\mu m} >80$ μmJy (grey open squares) and with $F_{24\mu m} >1$ mJy (green filled circles). The black, grey and green solid curves, from top to bottom, represent the median of all the 24 μm-selected sources with $F_{24\mu m} >80$ μJy, the median of the 24 μm-sources selected as DOGs with $F_{24\mu m} >80$ μmJy and the median of the brightest DOGs sources (i.e., with $F_{24\mu m} >1$ mJy), respectively. Errors on the median are calculated as quadratic propagation of uncertainty. We show the expected flux ratios (red dashed-triple dotted tracks) in the case that 25, 50 and 100% of the flux in the 100 μm band result from an AGN component (Mullaney et al. 2011, 2012). We also include for comparison the star-forming ULIRG CE01 templates for an IR luminosity of 10^{12} L$_\odot$ (bottom blue-dashed line) and $10^{12.5}$ L$_\odot$ (top blue-dashed line), as well as the template from Magdis et al. (2012) (light blue dotted-dashed line). The observed PACS/24 colors of the bulk of the 24 μm sources and that of the DOG sources are consistent with these ULIRG templates. *Right:* Distribution of $160\mu m/24\mu m$ color as a function of the redshift for all the 24 μm-selected sources detected at 160 μm (black open circles) and the 257 DOGs detected at 160 μm. The colors and tracks are the same as on the left panel. For clarity, we do not overplot the CE01 templates on the right panel as they would give the same results than for the 100/24 color.

4   AGN CONTRIBUTION TO THE TOTAL REST-FRAME 8-1000μM LUMINOSITY IN DOGS

Based on FIR/MIR colors, bright DOGs likely contain an AGN component, contributing partly or even dominating their IR luminosity. To have a better understanding of these sources and to have a global view of their stage in the evolution of the galaxies, it becomes important to know the exact contribution of a potential AGN to their total 8-1000μm rest frame luminosity. In this section we present our method to determine the potential contribution of an AGN component to these DOG sources and show our results on the variation in AGN contribution with the 24 μm flux.

4.1   Method: SED-fitting procedure

Studying the SED of a galaxy provides insights to the physical nature of the underlying continuum source and can unveil the presence of an AGN. The impact that an AGN contribution has on the shape of the SED is distinct from that of dust heated by star-forming activity. However, deriving the SED of a galaxy is not an easy exercise especially in the case of an AGN where the imprints of the host galaxy is always present. In our study we use the IDL-based SED-fitting procedure *DecompIR*, detailed in Mullaney et al. (2011). Combining a set of five starburst templates and an average AGN template, this approach is aimed at fitting the IR photometry of composite galaxies and to measure the AGN contribution to their total IR output. A χ^2 method is used to know which

combination of these templates best fits the data; i.e., the combination with the lowest associated χ^2 value is adopted as the best fit. The validity of this procedure as an accurate way to determine the AGN contribution to the total IR output of composite galaxies has been verified by several tests lead by Mullaney et al. (2011), including a comparison with alternative measures of the AGN contribution (e.g., emission line diagnostics). Although there are significant uncertainties associated to the precise AGN contribution to an individual galaxy, this approach is adequate from a statistical point of view (i.e., large samples, average SEDs).

We apply the *DecompIR* procedure to our sample of DOGs sources. Nonetheless, considering that DOGs have ULIRG-class luminosities (e.g., Bussmann et al. 2009; Riguccini et al. 2011), we add two ULIRGs templates with $L_{IR} = 10^{12} L_\odot$ and $L_{IR} = 10^{12.5} L_\odot$ to the set of starburst templates from Mullaney et al. (2011) to fully cover the luminosity range of our sample. The ULIRG templates are taken from CE01 as they build their library from SEDs and models that only take into account star formation activity. The median PACS/MIPS colors of the bulk of the DOGs sample are well represented by these ULIRGs templates (see Fig. 4), motivating their use as part of our SED-fitting procedure. To determine the AGN contribution to the IR luminosity of our sources, we first derive a best SED-fit with templates based only on star-forming sources. If the star-forming templates do not provide a satisfactory result, an AGN component is added and the SED-fitting proceeds with a composite spectra. We consider the AGN component as a

reasonable option only if it improves the χ^2 of the fit by at least 50%.

We implement our SED-fitting procedure to each DOG source in our sample. Each of the 95 sources are first fit by a star-forming component only and then by a composite spectra when the χ^2 from the star-forming fit is > 20. In the case of sources with a less-accurate photo-z, the source is fit with a star-forming template for all possible photo-zs obtained from the PDF (see Sect. 2.5). If none of these fits are suitable, we add an AGN component and the fits for each possible photo-z are performed once again. Our method is robust in fitting most of our sources (90%). Out of 95 DOGs, 71 are fit with a star-forming galaxy template only, 15 require an AGN component to the fit, and in 9 cases, no reliable fit was obtained either using a star-forming-only template nor a composite spectra. The failure of successfully fitting these sources could be due to the fact that we cannot reproduce the SED of these sources; this is most likely due to a wrong redshift, even after probing the different possibilities indicated by the PDF.

Due to the expected uncertainties on the AGN fraction for an individual galaxy, we implement the SED-fitting procedure to average DOG SEDs. We divide our DOG sample in 3 different redshift bins (1.5<z<2.0, 2.0<z<2.5 and 2.5<z<3.0) and in four 24 μm-flux bins (0.09< $F_{24\mu m}$ <0.24, 0.24< $F_{24\mu m}$ <0.65, 0.65< $F_{24\mu m}$ <1.76, and 1.76< $F_{24\mu m}$ <4.74 mJy). For each redshift bin and each 24 μm-flux bin, an averaged SED is calculated at 8 μm, 24 μm, 100 μm, 160 μm, 250 μm, 350 and 500 μm, leading to a total of 12 average SEDs. The results of the fits are shown in Fig 5 for the average SEDs and in Fig 6 & 7 for the individual sources fitted with an AGN.

The results from the SED-fitting procedure on the average DOG SEDs are presented on Table 2, including the AGN contribution to the total IR flux (f_{AGN}), the best-fit template and corresponding χ^2. Our method to get the AGN contribution does not appear to be biased toward one specific template. Independently of the AGN contribution, the two templates that were the most successful at fitting the average SEDs were the CE01 templates for IR luminosities of 10^{12} L$_\odot$ (CE12) and $10^{12.5}$ L$_\odot$ (CE12.5). This is as expected, since these templates have PACS/MIR colors consistent with that our DOG sources.

4.2 Results

We list the mid-to-far IR photometry and the total IR luminosity of the 95 Herschel-DOGs on Table 3, indicating also whether an AGN component is included as part of the SED fit. The redshift distribution of our DOG sample peaks at z~2, allowing us to use the 24 μm band as a probe of the mid-IR emission close to the rest frame 8 μm. This allows us to derive a $L_{8\mu m}$ that minimizes the dependence on the choice of SED template used to perform the k-corrections. To determine the rest-frame $L_{8\mu m}$ we interpolate the CE01 library at the redshift and flux of each average SED. We are then in a position to study the fractional AGN contribution to the total 8-1000 μm output as a function of the 8μm rest-frame luminosity ($L_{8\mu m}$); we do this for the average SEDs at the three redshift bins: $z = 1.5 - 2.0$, $2.0 - 2.5$ and $2.5 - 3.0$ (see Fig. 8).

We find that the AGN contribution increases globally with increasing $L_{8\mu m}$ for all our redshift bins (see Fig. 8). This confirms the findings of Pope et al. (2008), where they report – based on mid-IR colors of 79 sources within the GOODS field and with 24 μm fluxes down to 100 μJy – that low-luminosity DOGs are primarily powered by star-formation activity. However, only MIPS-70μm observations were available for their analysis and the inability to sample properly the peak of the SED lead to large uncertainties on the derivation of the dust temperature and the AGN contribution; Penner et al. (2012) extend the study out to far-IR wavebands but miss the faintest DOGs by focussing on GOODS DOGs with luminosities 10^{12} L$_\odot$ < L$_{IR}$ < 10^{13} L$_\odot$. Furthermore, Fiore et al. (2008) claimed that even faint DOGs show evidence of hard X-ray emission, suggesting the presence of an underlying AGN contribution. Within this context our work – based on the large 2 deg^2 area of the COSMOS field and the good sensitivity of the MIPS-24 μm observations that allows us to sample a wider range of 24 μm fluxes (i.e, 80 μJy < $F_{24\mu m}$ < 5 mJy) and the access of far-IR data with *Herschel* – allows us to conclude that faint DOGs are mainly star-forming systems while brighter sources become dominated by an AGN.

By separating our sample in redshift bins, Fig. 8 also shows that the relation between AGN fraction and $L_{8\mu m}$ evolves with redshift: the slope of the AGN contribution with respect to the $L_{8\mu m}$ is steeper at low redshifts, while at higher redshifts the AGN contribution is less important. This is consistent with the results from Merloni & Heinz (2008), where they find that although the accretion rate density onto supermassive black holes (SMBH) and star-formation rate (SFR) densities increase from $z \sim 0$ to then decrease beyond z~2, the decrease in SMBH activity is sharper than that of the SFR. We note that the uncertainties on the derived AGN contributions are calculated from the formal error output resulting from the χ^2 in the SED-fitting procedure.

In the interest of studying the star formation activity in our sources, we use the results from our SED decomposition to extract the AGN contribution and calculate IR luminosities only due to star formation. The resulting values span the range of 10^{11} L$_\odot$ < L$_{IR}$ < 10^{13} L$_\odot$, corresponding to one order of magnitude fainter than the analysis by Penner et al. (2012). We study these IR luminosities as a function of the rest-frame 8μm luminosity and find that for a given 8μm luminosity DOG sources whose SEDs are best fit with the addition of an AGN component exhibit significantly lower IR luminosities than DOGs fit with a host-only component (see Fig. 9, top panel). In fact, for a given 8μm luminosity the majority (~75%) of DOGs fit by a host-only component display similar IR luminosities to the median star-forming galaxies within the GOODS-Herschel sample from Elbaz et al. (2011), while AGN-DOGs populate the lower-tail of IR-to-8μm luminosity ratios (IR8 = L$_{IR}$/L$_{8\mu m}$; see Fig. 9, bottom panel). We observe an anti-correlation between the IR8 ratio and the $L_{8\mu m}$ with the AGN-DOGs populating the brightest $L_{8\mu m}$-end.

For each DOG source in our sample we convert the IR luminosity into SFR according to Kennicutt (1998) and adopt the stellar mass from Ilbert et al. (2009). We consider the redshift evolution of the specific SFR (sSFR = SFR/M$_*$) of our DOG sample and find that the majority of DOGs with no AGN component display sSFRs that place them at
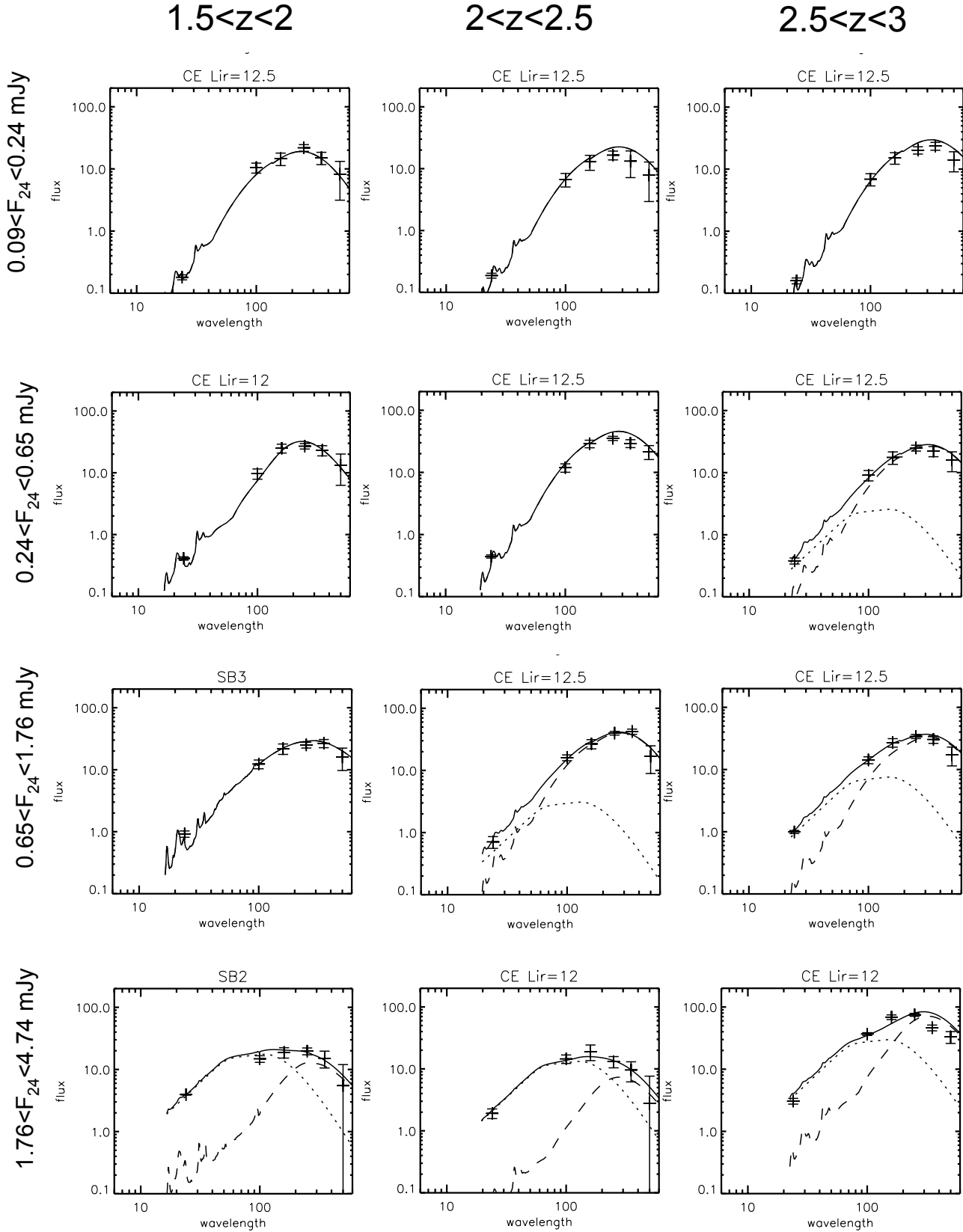
Figure 5. SEDs of the 12 average templates of DOGs galaxies from our sample. The solid line corresponds to the total SED fit, the dashed line is the host template and the dotted line is the AGN component. The name of the template used is written on each panels. The flux bins are specified on the left side and the redshift bins are written on the top.

Table 2. Results from the SED-fitting for the average SEDs per redshift bins and per flux bins. f_{AGN} is the percentage of total 8-1000μm flux that comes from AGN. We specify the star-forming template best fitting the host galaxy (SB for the starburst templates from (Mullaney et al. 2011) and CE 12.5 and CE 12 for the CE01 ULIRG templates.

| Redshift	Flux (mJy)	f_{AGN} %	error %	Template (Host galaxy)	χ^2	L_{ir} $L_\odot$
1.5<z<2.0	0.09<f<0.24	0	–	CE 12.5	4.4	9.60e+11
	0.24<f<0.65	0	–	CE 12	5.3	1.29e+12
	0.65<f<1.76	0	–	SB3	5.3	1.69e+12
	1.76<f<4.74	83	3.5	SB2	6.5	2.42e+12
2<z<2.5	0.09<f<0.24	0	–	CE 12.5	6.9	1.50e+12
	0.24<f<0.65	0	–	CE 12.5	34.6	3.05e+1
	0.65<f<1.76	17	5.6	CE 12.5	0.8	5.52e+11
	1.76<f<4.74	86	15.7	CE 12	0.8	2.43e+12
2.5<z<3.0	0.09<f<0.24	0	–	CE 12.5	21	2.42e+12
	0.24<f<0.65	20	3.5	CE 12.5	0.4	5.60e+11
	0.65<f<1.76	38	3.2	CE 12.5	0.1	1.69e+12
	1.76<f<4.74	59	4.5	CE 12	13	6.68e+12

le
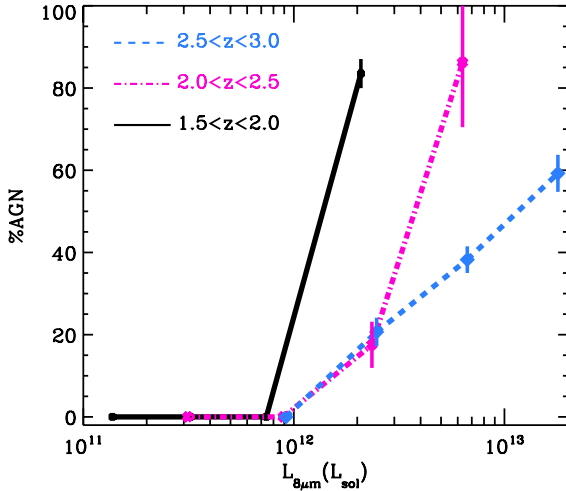
Figure 8. Evolution of the contribution of the AGN component to the total rest-frame 8-1000μm flux of the sources as a function of the 8μm rest-frame luminosity ($L_{8\mu m}$). The AGN fraction is given for 3 different redshift bins: 1.5<z<2.0 (solid black line), 2.0<z<2.5 (pink dot-dashed line) and 2.5<z<3.0 (bleu dashed line). The AGN contribution is obtained from the fitting procedure described in Sect. 4 on the 12 average SED (see Table 2). The general trend is an increasing contribution of the AGN component with respect to the $L_{8\mu m}$ of the source irrespective of the redshift range.

or above the main sequence (MS) from Elbaz et al. (2011), while 50% of the AGN-DOGs show significantly lower sSFR values (i.e., they lie below the MS)(see Fig. 10). Sources that lie a factor of 2 above the MS are considered as "starbursts" by Elbaz et al. (2011). All but three host-component galaxies lie within a factor of 2 around the MS or in the starburst's zone. The distribution in sSFRs shown in Fig. 10 highlights the composite nature of the DOG population: some DOGs are dominated by starburst activity, the majority is undergoing star-formation as part of the MS, while others are domi-

nated by an AGN. This prompts the idea that DOGs are at the crossroads of the ULIRG-quasar scenario proposed by (Sanders et al. 1988a,b; Bussmann et al. 2012), with AGN-DOGs being closer to a quasar phase, where the AGN has already started to quench the star formation (explaining the lower sSFR observed on Fig. 10).

4.3 Comparison with IRAC-color AGN selection criteria

Our SED-fitting analysis identifies 15 Herschel-detected DOGs with an important AGN contribution to the total IR output. We compare our AGN classification of DOGs to prior approaches relying on an IRAC-color selection. Fig. 11 shows the IRAC-color selection of AGNs by Lacy et al. (2004), as well as the refined IRAC-color selection of Donley et al. (2012), which also includes a power-law criteria in the mid-IR: $S_{3.6} < S_{4.5}$ and $S_{4.5} < S_{5.8}$ and $S_{5.8} < S_{8.0}$.

The majority of our sources display IRAC colors consistent with the criteria of Lacy et al. (2004), which would suggest that 90% of our DOGs are AGNs. However, our SED-fitting analysis indicates that only ∼15% of our sources have a large AGN contribution. Based on this we conclude that relying on the AGN criteria of Lacy et al. (2004) would lead to a lack of precision in selecting AGNs versus galaxies dominated by star formation. On the other hand, more than 50% of our AGN-DOGs lie within the Donley et al. (2012) criterion, suggesting that it is a more reliable way of selecting AGNs in DOGs when considering merely IRAC colors. However, from the 19 DOGs that lie within the AGN-criteria of Donley et al. (2012) – and excluding the 3 that do not follow the power-law criteria required by the authors – only 9 are classified as AGNs following our SED-fitting analysis. That is, 40% of the Herschel-DOGs with IRAC colors consistent with the criterion of Donley et al. (2012) do not have a significant AGN contribution according to our analysis. Of particular interest is that out of all our AGN-DOGs, six (i.e., ∼40%) are not identified as AGNs based on the crite-
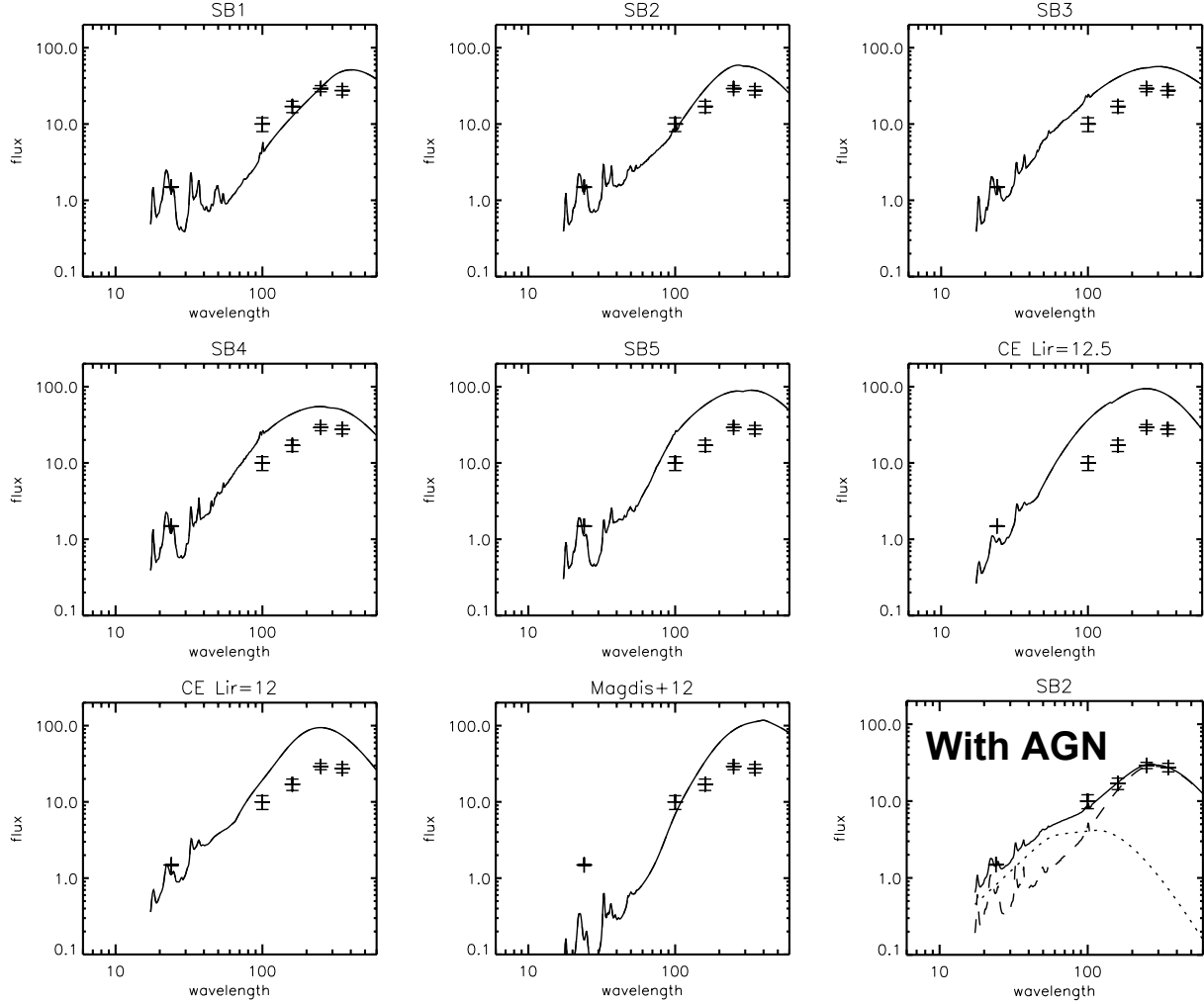
Figure 6. Following the same format as Fig. 5, this figure shows the results of the SED-fitting procedure for DOG80, one of the 15 DOGs which require an AGN component: the first 7 panels are the results of the SED-fitting with a host component only and the last panel (bottom middle panel) is the acceptable fit, with a contribution of an AGN component ($20\% < f_{AGN} < 40\%$).

ria by Donley et al. (2012), four of which do not follow the power-law criterion required.

On the one hand, our AGN classification is based on the availability of far-IR data for obscured sources such as DOGs. On the other, Lacy et al. (2004) and Donley et al. (2012) classify sources as AGN-dominated based on IRAC-color selections. When considering these selections side by side, we draw two main conclusions: (1) non PL-DOGs potentially host an AGN that may dominate the far-IR regime even when missed by the IRAC-color selection criteria of Lacy et al. (2004) and Donley et al. (2012); and (2) PL-DOGs with an AGN according to our SED-fitting procedure can be missed by IRAC colors criteria. We conclude that our method provides an alternate means of determining the composite nature of DOGs.

5 DUST TEMPERATURES AND MASSES

It has been well established that interstellar dust absorbs a large fraction of the UV/optical radiation from DOGs and reemits it in the IR (Penner et al. 2012) As such, it is essential that we understand the dust properties of these galaxies if we are to understand this potentially-important population of galaxies. In this section, we derive the dust temperatures and masses for our sample of DOGs. The availability of far-IR data from *Herschel* is crucial to obtain these properties. We are now able to extend previous studies on DOGs that did not have access to such high-quality far-IR data (e.g., Dey et al. 2008; Bussmann et al. 2009, 2012). We are also in a position to compare results with other recent studies using (limited) *Herschel* data on DOGs, including that of SPIRE-detected sources (down to only $F_{24\mu m} > 0.3\,\mathrm{mJy}$) with spectroscopic redshifts in the Bootes field by Melbourne et al. (2012) and the study by Calanog et al. (2013) on SPIRE-detected DOGs within COSMOS; no PACS data were available for either study.
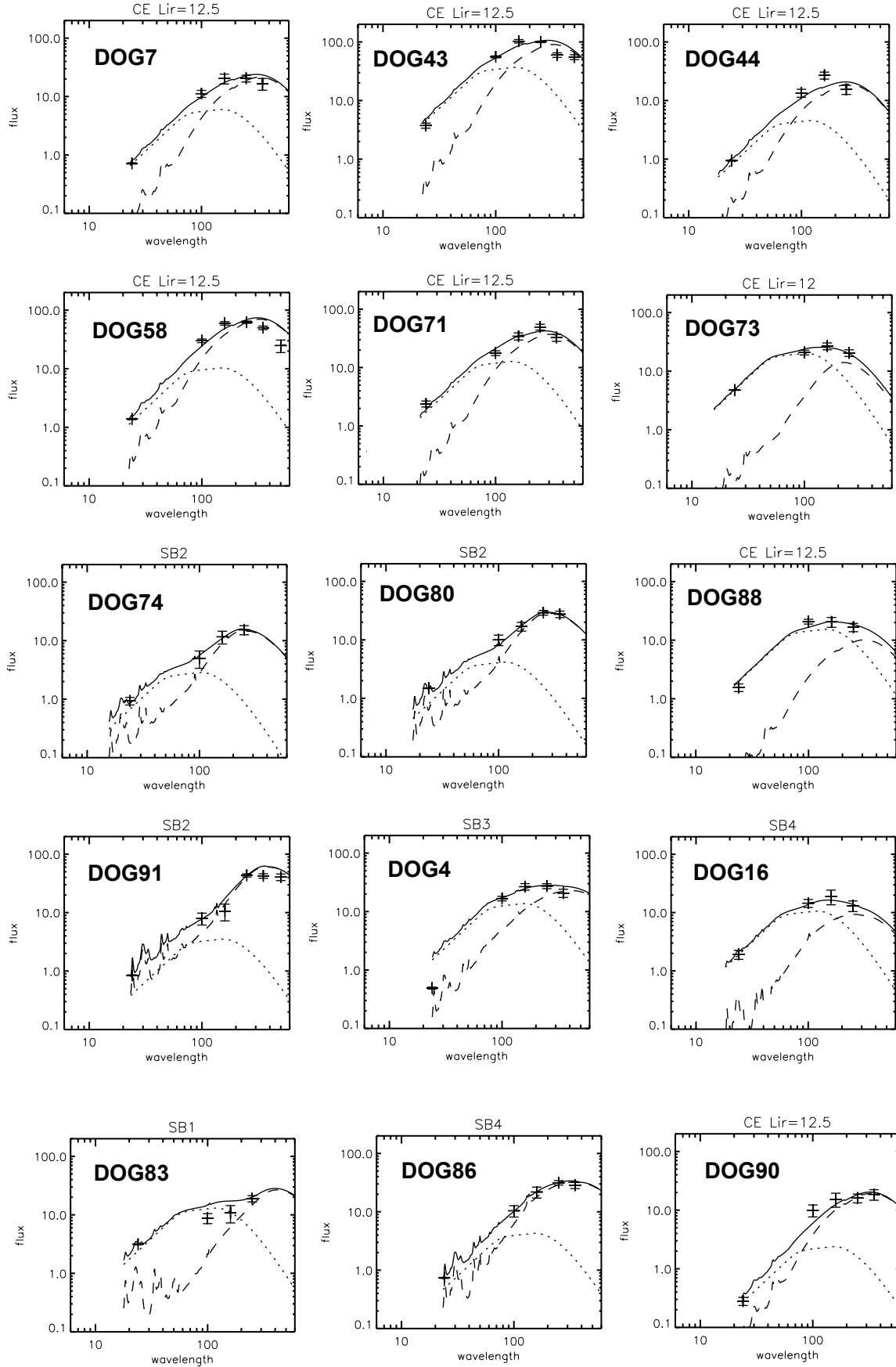
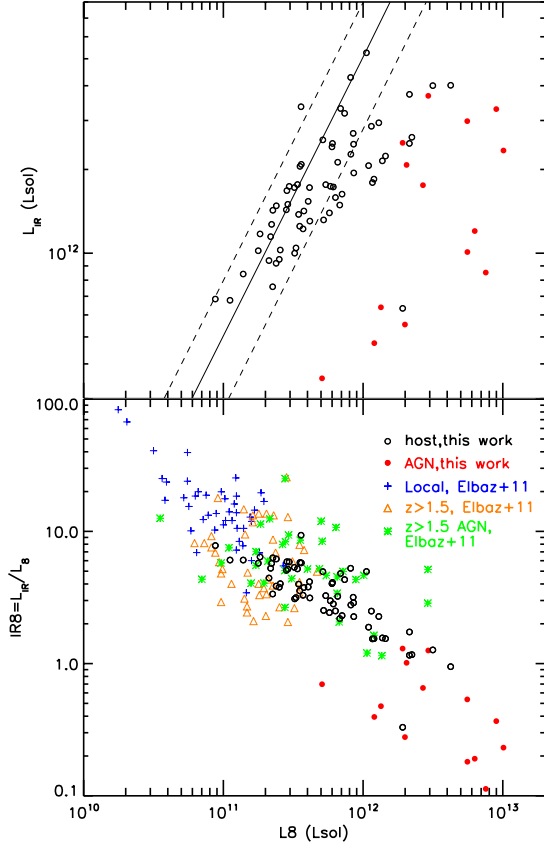**Figure 7.** Similar to Fig. 5, SEDs of the 15 DOGs which require the contribution of an AGN component.

Figure 9. *Upper panel:* Comparison of L_{IR} with L_8 (rest-frame 8 μm) for DOGs from our sample (galaxies with host component only are marked with black open circles and AGNs are marked with red filled circles). For comparison, we show the median location of star-forming galaxies from Elbaz et al. (2011) (solid line), with the dashed lines showing the 68% dispersion. *Lower panel:* Variation of the IR8 (=L_{IR}/L_8) ratio with the 8μm luminosity for our DOG sample, following the same color code as in the upper panel. For comparison we also plot galaxies from Elbaz et al. (2011), including local galaxies (blue crosses), star-forming galaxies at z>1.5 (orange triangles) and AGNs at z>1.5 (green asterisk). See text for details.

5.1 The Single Temperature Model

The availability of *Herschel* far-IR data allows us to constrain the peak of the SED in the far-IR regime and to calculate the dust masses and temperatures of our galaxies with a higher accuracy than previous studies. DecompIR does not provide information on the dust amount of our sources; we fit a blackbody spectrum B_ν of temperature T using far-IR data (see Amblard et al. 2014). To summarize, we perform a single temperature fit (hereafter 1T model) with an emissivity, β, of 1.5 to fluxes long ward of $\lambda_{rest-frame} > 40\,\mu$m. The luminosity is then expressed as

$$L(\nu) \propto B(\nu, T_d)\nu^\beta. \tag{1}$$

Considering $\lambda_{rest-frame} > 40\,\mu$m, we avoid emission from the AGN that can boost the dust temperature and bias our results (Netzer et al. 2007; Mullaney et al. 2011). For this reason we restrict ourselves to using only the PACS 100, 160 μm and SPIRE 250, 350, 500 μm bands for galaxies with
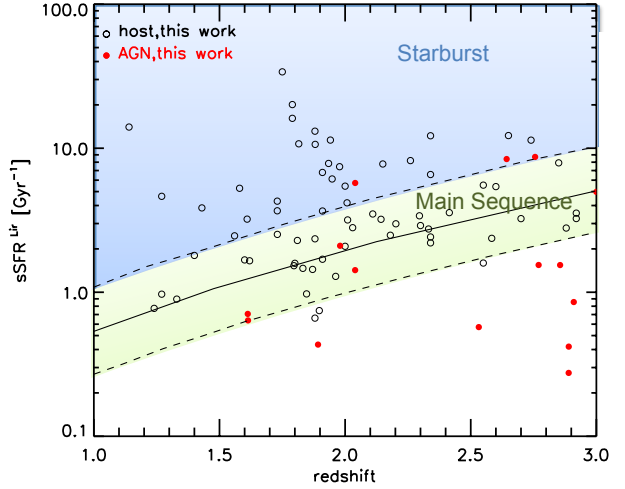

Figure 10. Redshift evolution of the specific SFR (sSFR = SFR/M_*) of DOGs; we distinguish between DOG sources whose SEDs are best fit with a host-only component (black open circles) and with the addition of an AGN component (red filled circles). The solid line represents the star-forming main sequence from Elbaz et al. (2011) and the dashed lines are a factor 2 above and below this fit. See text for details.
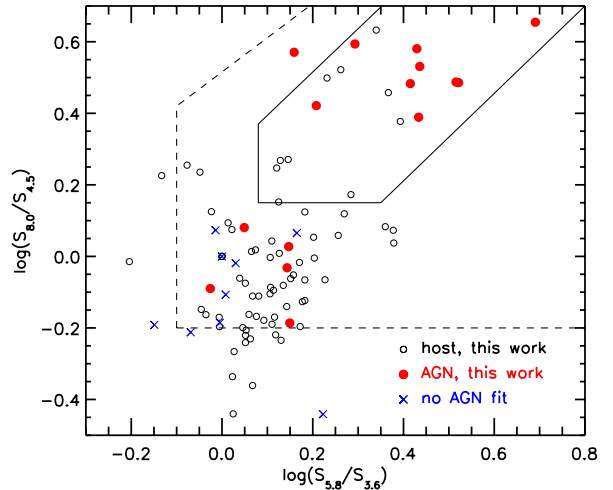

Figure 11. IRAC colors of host-component DOGs (black open circles) and of the AGN-DOGs (red filled circles) from this work ; we also indicate the IRAC colors of the 9 sources for which no SED fit was possible (blue crosses; see Sect. 4.3 for details). The solid line box is the AGN selection criterion from Donley et al. (2012) and the wider dashed box is from Lacy et al. (2004).

z<1.7 and only the SPIRE 250, 350, 500 μm bands (when available) for z>1.7 galaxies. We require a minimum of 3 data points to fit the SED. At z<1.7, 15 DOGs comply with this requirement (from the 16 DOGS at z<1.7). At z>1.7, from the 24 sources that have SPIRE fluxes above the 3–σ limit, 22 have 3 data points.

We enforce the dust temperature to be constrained between 10 and 95 K, the luminosity between 10^{10} and 10^{14} L$_\odot$, acknowledging the high luminosities of our sample
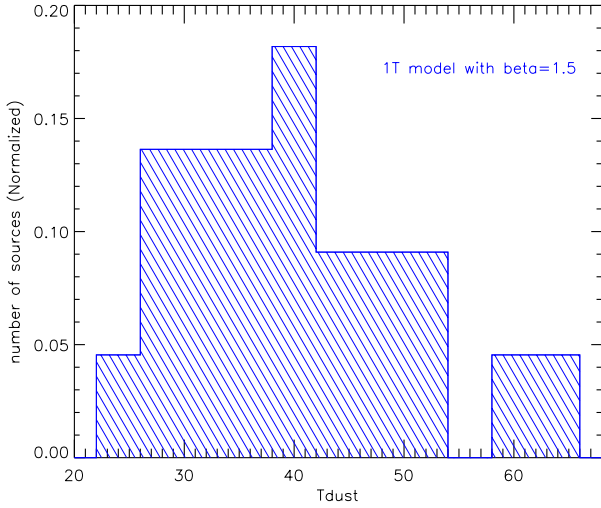
Figure 12. Distribution of the dust temperature of the 24 DOGs with a detection in the 3 SPIRE bands with the 1T model (22 sources at z> 1.7 and 2 sources at lower redshifts). The dust temperature peaks at $T_d \sim 40$ K and is comprised within the range $24 < T_{dust} < 65$ K.

(see Fig. 9). We observed the same definition as Amblard et al. (2014) for the dust luminosity and for the dust mass :

$$L_d(\lambda) = 4\pi M_d \kappa(\lambda) B(\lambda, Td) \qquad (2)$$

$$M_d = L_d / \int 4\pi \kappa(\lambda) B(\lambda, T) d\lambda \qquad (3)$$

where κ is taken at 850 μm (Dunne et al. 2000) and equal to 0.077 kg^{-1}/m^2 (Draine & Lee 1984; Hughes et al. 1993).

We find a median dust temperature of $T_d \sim (40.6 \pm 9.2)$ K for our sample. The dust temperatures of our DOGs are in overall good agreement with estimates from the literature for other samples of DOGs. Bussmann et al. (2009) predicted a high dust temperature for DOGs sources with $T_d > 35$-60 K, but this estimate was mainly based on observed wavelengths shortward of $\sim 350 \mu$m: only 4 of their 12 DOGs have 350μm fluxes, the rest of the sample has only upper limits). Melbourne et al. (2012) find lower dust temperatures for their *Herschel*-detected DOG sources (i.e., $20 < T_d < 40$ K). They split their sample into bump DOGs and PL-DOGs and find that the PL-DOGs are less likely to be detected at far-IR wavelengths using SPIRE than the bump DOGs. They also claim that SPIRE detections are biased towards very cold sources. We note that our range of temperature (~ 24-65 K) is wider than that of Melbourne et al. (2012). Our dust temperatures are in good agreement with Calanog et al. (2013, within uncertainties) : they find $T_d = (37 \pm 6)$ K for detected PL-DOGs and $T_d = (35 \pm 7)$ K for detected bump sources. As raised in the literature (e.g., Melbourne et al. 2012), using only SPIRE data tends to underestimate the dust temperature. Therefore, we need to be cautious in our analysis since more than half of our dust temperatures are obtained using only SPIRE data.
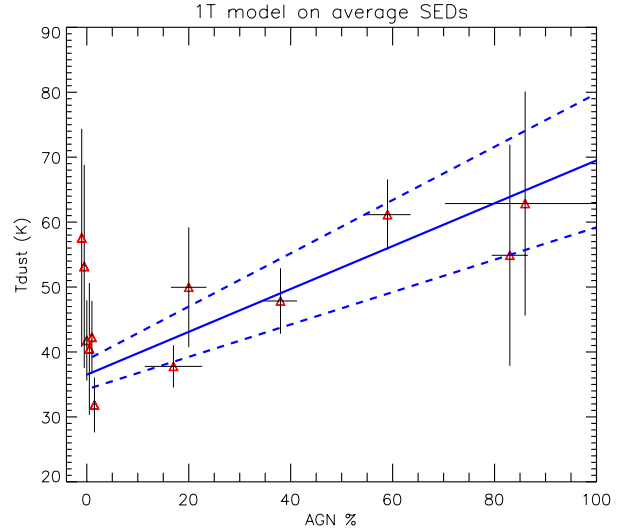

Figure 13. Evolution of the dust temperature obtained with the 1T model as a function of the AGN fraction. The results are obtained for the 12 average SEDs presented in Table 2 and detailed in Sec. 4.1. To improve clarity, we have slightly changed the x values for the 6 points with no AGN fraction in order to exhibit more clearly the error bars on the figure. The blue line is the best χ^2 fit with a slope of 0.33±0.08 for the 6 average SEDs with an AGN contribution. The dotted lines represent the 1σ error.

5.2 Discussion

5.2.1 *Effect of the AGN contribution on the dust temperatures*

With the goal of improving our accuracy in deriving dust temperature and mass, we use the average SEDs obtained per bin of 24 μm fluxes and per bin of redshift (see Sec. 4.1 and in Table 2 for details) instead of the SEDs of individual DOG sources. The dust temperatures have been derived for the average SEDs following the procedure described in Sec. 5.1. These are presented in Fig. 13 as a function of AGN fractional contribution. Roughly half of the average SEDs have no AGN contribution and show a wide range of T_d as seen on the left side of Fig. 13. The two sources with no AGN fraction and with the highest dust temperatures show extremely large errors bars on the dust temperature (i.e. ± 15 K and ± 16 K) while the average dust temperature error for the sample is around 9 K. The rest of the average SEDs have an AGN contribution ranging from 20% to almost 90% and are within the same T_d range as the sources with no AGN component. The DOGs' average SEDs with an AGN contribution display a correlation between the AGN contribution and the dust temperature. We perform a best-χ^2 fit on the 12 data points, taking into account the errors both on the x and y axes and find a slope of 0.33±0.08 with a reduced χ^2 of 0.94. To insure the validity of our fitting method, we also perform a fit T = cste with

$$cste = \frac{\Sigma T / \sigma_T{}^2}{\Sigma 1 / \sigma_T{}^2} = 42.6\,K.$$

The reduced χ^2 for this flat fit being 2.53, this gives us a strong indication that our previous fit is valid. We also estimate the Spearman's (rho) rank correlation of T_{dust} and

the AGN percentage. The significance is low (0.04), which indicates a significant correlation. The correlation between the dust temperature and the AGN percentage for the average SEDs with AGN contribution is thus real, even though the slope is small. However, we do not confirm the presence of a general trend between the AGN fraction and the dust temperature of the sources since half of the data points with no AGN activity present similar dust temperatures than the average SEDs with a large contribution from an AGN.

5.2.2 *Effect of the AGN contribution on the dust masses*

In addition to dust temperatures, the 1T model fitting procedure also provides us with the dust masses of our sample sources. We obtain a range for the entire sample of $7 \times 10^7 < M_{dust} < 10^9 \, M_\odot$ and a median dust mass of $\sim (3 \pm 3) \times 10^8 \, M_\odot$. Our results are in very good agreement with Bussmann et al. (2009) who found a median dust mass of $3 \times 10^8 \, M_\odot$ for their sample of 31 of the brightest DOGs ($F_{24\mu m} > 0.8$ mJy) in the Bootes Field and with HST imaging. Their sample is dominated by sources with a power law in the mid-IR IRAC bands, which is a signature of the presence of an AGN (Donley et al. 2007).

DOGs are believed to be an intermediate AGN phase between high-redshift sub millimeter galaxies (SMGs) and quasars at z∼2 (Bussmann et al. 2012). Accounting for uncertainty in κ which could be as much as a factor of three, the median dust mass of our sample is not different from those estimated for high-redshift SMGs by Magnelli et al. (2012b) ($M_d \sim 10^9 \, M_\odot$). Pope et al. (2008) found that 30 % of the SMGs from their sample also satisfy the DOG criteria, and of those SMG-DOGs, 30 % are AGN dominated. DOGs could then be the descendants of these SMGs with similar dust content, but representing a more advanced AGN-phase than could later quench the star-formation and lead to elliptical galaxies.

6 SUMMARY AND CONCLUSIONS

We carry out a study that aims to understand the composite nature of 24μm-bright Dust-Obscured Galaxies (DOGs). These sources are a subset of ULIRGs at high redshift ($z \sim 2$) with $F_{24\mu m}/F_R > 982$. ULIRGs are considered to represent an important phase in the evolution of galaxies as they are linked to the formation of massive galaxies via gas-rich starbursting mergers followed by an AGN-driven quenching of the star-formation (e.g., Sanders et al. 1988a,b). Recent studies (Dey et al. 2008; Bussmann et al. 2009, 2012) have suggested a similar evolutionary sequence where DOGs are an important intermediate phase between gas-rich major mergers (traced by submillimeter galaxies, SMGs) and quasars at z∼2. These studies describe an evolutionary scenario in which the starbursting nature of SMGs evolves into the composite nature of DOGs as an underlying AGN grows; this is followed by a quasar phase that terminates star formation, leading to the formation of a passive, massive elliptical galaxy. Within this context, DOGs could provide a key insight to an extremely dusty stage in the evolution of galaxies at $z \sim 2$, where both AGN and star formation activity coexist. Their composite nature was un-

til relatively recently inaccessible prior to the availability of sensitive mid- to far-infrared data.

We base our work on a sample of 95 *Herschel*-detected DOG sources. We perform SED-fitting on our sources using composite spectra to obtain AGN contributions, dust temperatures and dust masses. We summarize below our results and our conclusions:

(i) DOGs with the brightest 24μm fluxes ($F_{24\mu m} > 1$ mJy) present significantly bluer PACS/24μm colors than other 24μm-selected sources. These bluer colors may be explained by templates containing an AGN contribution of at least 25%.

(ii) Among our sample of 95 sources, 74% are fit by a host galaxy template while for 16% require an additional AGN component. The remaining 10% of the sample could not be properly fit, likely due to inaccurate photometric redshifts.

(iii) Faint DOG sources with $L_{8\mu m} < 10^{12} \, L_\odot$ are dominated by star-formation at all redshifts, while DOGs brighter than $L_{8\mu m} > 2 \times 10^{12} \, L_\odot$ display a high contribution (>20%) from an AGN component.

(iv) DOGs with no significant AGN contribution are mainly located within the star-forming main sequence as defined in Elbaz et al. (2011). Those identified as AGN-DOGs present the lowest IR8 ($= L_{IR}/L8$) ratio of our sample and 50% of them lie below this sequence, with significantly lower specific star-formation rates. This results support the evolutionary scenario where DOGs may represent a transition phase between high-redshift starburst-dominated SMGs and red-dead ellipticals, passing through an AGN-phase that would quench star formation.

(v) The dust temperature of DOGs peaks at (40 ± 9) K and our range of temperatures ($24 < T_d < 65$ K) is overall in good agreement with the literature (Bussmann et al. 2009, 2012; Melbourne et al. 2012; Calanog et al. 2013). DOGs with a contribution from an AGN in the far-IR of at least 60 % have dust temperatures >50 K, suggesting that the AGN heats the dust of its host galaxy. We find a median dust mass of $\sim (3 \pm 3) \times 10^8 \, M_\odot$ for our sample consistent previous analysis in the literature (Bussmann et al. 2012).

This work sheds light on DOG sources and their underlying composite nature, bringing unequivocally to light that mid-IR bright DOGs are powered by an AGN. The submillimeters facilities in the near future, such as CCAT and ALMA will provide critical insight to study the AGN properties of these obscured ULIRGs at z∼2.

This paper is the first of a series on the panchromatic view of DOGs. In this paper we focus on their far-IR properties, while in the upcoming papers we will focus on their X-ray properties based on X-ray stacking analysis and on their contribution to the Cosmic X-ray Background. The far-IR/radio correlation of these sources and their radio properties using JVLA-COSMOS observations presented in Smolčić et al. (2014) will be detailed in a forthcoming paper.

This paper has been typeset from a TEX/ LATEX file prepared by the author.

REFERENCES

Amblard A., Riguccini L., Temi P., Im S., Fanelli M., Serra P., 2014, ApJ, 783, 135
Berta S. et al., 2011, A&A, 532, A49
Brinchmann J., Charlot S., White S. D. M., Tremonti C., Kauffmann G., Heckman T., Brinkmann J., 2004, MNRAS, 351, 1151
Brusa M. et al., 2010, ApJ, 716, 348
Brusa M. et al., 2007, ApJs, 172, 353
Bussmann R. S. et al., 2012, ApJ, 744, 150
Bussmann R. S. et al., 2009, ApJ, 705, 184
Calanog J. A. et al., 2013, ApJ, 775, 61
Capak P. et al., 2007, ApJs, 172, 99
Chary R., Elbaz D., 2001, ApJ, 556, 562
Daddi E. et al., 2007, ApJ, 670, 156
Desai V. et al., 2009, ApJ, 700, 1190
Dey A. et al., 2008, ApJ, 677, 943
Donley J. L. et al., 2012, ApJ, 748, 142
Donley J. L., Rieke G. H., Pérez-González P. G., Rigby J. R., Alonso-Herrero A., 2007, ApJ, 660, 167
Draine B. T., Lee H. M., 1984, ApJ, 285, 89
Dunne L., Eales S., Edmunds M., Ivison R., Alexander P., Clements D. L., 2000, MNRAS, 315, 115
Elbaz D. et al., 2011, A&A, 533, A119
Elbaz D. et al., 2010, A&A, 518, L29
Elvis M. et al., 2009, ApJs, 184, 158
Farrah D. et al., 2008, ApJ, 677, 957
Fiore F. et al., 2008, ApJ, 672, 94
Fiore F. et al., 2009, ApJ, 693, 447
Griffin M. J. et al., 2010, A&A, 518, L3
Hasinger G. et al., 2007, ApJs, 172, 29
Houck J. R. et al., 2005, ApJl, 622, L105
Hughes D. H., Robson E. I., Dunlop J. S., Gear W. K., 1993, MNRAS, 263, 607
Ilbert O. et al., 2009, ApJ, 690, 1236
Kennicutt R. C., 1998, ARA&A, 36, 189
Lacy M. et al., 2004, ApJs, 154, 166
Le Floc'h E. et al., 2009, ApJ, 703, 222
Le Floc'h E. et al., 2005, ApJ, 632, 169
Lilly S. J. et al., 2007, ApJs, 172, 70
Lutz D. et al., 2011, A&A, 532, A90
Magdis G. E. et al., 2012, ApJ, 760, 6
Magdis G. E., Rigopoulou D., Huang J.-S., Fazio G. G., 2010, MNRAS, 401, 1521
Magnelli B., Elbaz D., Chary R. R., Dickinson M., Le Borgne D., Frayer D. T., Willmer C. N. A., 2009, A&A, 496, 57
Magnelli B. et al., 2012a, A&A, 539, A155
Magnelli B. et al., 2012b, A&A, 548, A22
McCracken H. J. et al., 2010, ApJ, 708, 202
Melbourne J. et al., 2009, AJ, 137, 4854
Melbourne J. et al., 2012, AJ, 143, 125
Merloni A., Heinz S., 2008, MNRAS, 388, 1011
Mullaney J. R., Alexander D. M., Goulding A. D., Hickox R. C., 2011, MNRAS, 414, 1082
Mullaney J. R. et al., 2012, MNRAS, 419, 95
Netzer H. et al., 2007, ApJ, 666, 806
Nguyen H. T. et al., 2010, A&A, 518, L5
Nordon R. et al., 2012, ApJ, 745, 182
Nordon R. et al., 2010, A&A, 518, L24
Oliver S. J. et al., 2012, MNRAS, 424, 1614
Pannella M. et al., 2009, ApJl, 698, L116
Penner K. et al., 2012, ApJ, 759, 28
Pilbratt G. L. et al., 2010, A&A, 518, L1
Poglitsch A. et al., 2010, A&A, 518, L2
Pope A. et al., 2008, ApJ, 689, 127
Riguccini L. et al., 2011, A&A, 534, A81
Roseboom I. G. et al., 2010, MNRAS, 409, 48
Salvato M. et al., 2009, ApJ, 690, 1250
Sanders D. B. et al., 2007, ApJs, 172, 86
Sanders D. B., Soifer B. T., Elias J. H., Madore B. F., Matthews K., Neugebauer G., Scoville N. Z., 1988a, ApJ, 325, 74

Table 3. DOGs sample

DOG ID	redshift	F_{24} (mJy)	F_{100} (mJy)	F_{160} (mJy)	F_{250} (mJy)	F_{350} (mJy)	F_{500} (mJy)	flag AGN	χ^2	L_{ir} ($L_\odot$)
0	1.87	0.386	9.798	14.33	35.05	17.40	14.67	0	2.90	1.02e+12
1	1.60	0.178	11.48	10.53	23.54	16.14	10.17	0	9.59	8.41e+11
2	2.65	0.176	9.251	11.81	21.27	19.14	14.26	0	6.22	3.41e+12
3	2.34	0.491	16.73	26.67	27.36	20.72	7.077	0	3.00	2.48e+12
4	3.00	0.097	9.961	27.31	25.93	14.49	3.826	3	0.409	3.67e+12
5	1.00	0.404	9.088	20.96	12.49	8.223	6.096	0	37.8	1.30e+12
6	1.40	0.440	7.806	16.88	15.89	13.25	9.133	0	20.5	6.84e+11
7	2.85	0.326	8.145	13.69	22.02	18.26	5.261	2	2.19	1.20e+12
8	2.34	0.402	8.467	24.79	22.32	20.23	9.081	0	3.00	2.48e+12
9	1.89	0.312	15.11	10.92	10.72	10.60	8.063	0	7.78	1.49e+12
10	1.14	0.103	5.576	16.27	15.17	17.43	5.545	0	3.56	4.15e+11
11	1.98	0.156	14.28	18.67	25.49	17.19	2.676	-99	-99	-99
12	1.88	0.236	11.65	29.26	19.52	7.441	3.868	0	24.5	1.587e+12
13	1.81	0.444	14.62	43.96	31.01	17.75	7.619	0	0.0739	9.502e+11
14	1.79	0.201	6.918	32.55	30.33	19.84	9.915	0	31.7	2.460e+12
15	2.30	0.326	8.989	18.93	30.08	21.45	20.49	0	8.01	2.068e+12
16	2.04	0.656	9.732	20.43	30.88	34.16	15.04	4	0.668	1.753e+12
17	2.34	0.716	11.18	20.34	20.45	16.57	8.984	0	0.311	1.760e+12
18	2.88	0.330	17.99	54.18	43.51	35.79	32.05	0	12.6	4.012e+12
19	2.74	0.223	12.73	22.93	32.10	20.40	5.487	0	0.509	4.354e+12
20	2.41	0.665	16.44	27.88	17.78	14.48	0.769	0	2.57	1.842e+12
21	1.90	0.363	6.506	9.178	21.98	19.80	13.77	0	4.31	1.538e+12
22	2.15	0.319	9.573	31.35	50.37	43.09	29.44	0	29.9	1.798e+12
23	2.11	0.400	9.302	26.70	34.57	26.41	13.75	0	15.8	2.122e+12
24	2.14	0.208	5.767	15.81	18.79	12.01	5.824	0	32.7	2.412e+12
25	2.50	0.414	4.650	14.08	35.78	28.10	10.19	-99	-99	-99
26	2.29	0.485	7.434	15.55	26.60	25.71	25.31	0	9.11	3.31e+12
27	1.84	0.285	7.054	23.17	24.96	21.93	9.473	0	5.71	9.19e+11
28	1.79	0.400	7.824	16.42	12.27	14.91	6.783	0	3.61	1.59e+12
29	1.80	0.532	7.399	21.88	28.97	24.07	13.26	-99	-99	-99
30	1.91	0.287	8.802	23.61	27.99	26.50	17.52	0	2.37	1.14e+12
31	1.80	0.601	10.28	32.24	50.22	57.26	37.58	0	0.503	1.67e+12
32	1.43	0.271	27.75	50.52	54.32	22.67	22.84	0	47.8	1.42e+12
33	1.24	0.405	7.274	12.76	24.40	25.07	12.53	0	0.0981	6.33e+11
34	1.73	0.090	3.589	13.36	18.04	8.671	1.258	0	1.04	1.04e+12
35	1.83	0.669	7.372	18.38	29.18	21.97	15.27	0	3.06	1.73e+12
36	1.88	0.388	12.93	17.25	11.61	5.563	3.736	0	13.3	1.63e+12
37	2.18	0.185	11.57	16.36	20.27	11.07	7.944	0	4.96	2.85e+12
38	1.68	0.846	7.959	10.58	43.39	42.47	40.47	0	2.16	9.40e+11
39	1.56	0.280	9.949	15.29	16.03	18.52	12.97	0	10.0	1.25e+12
40	1.71	0.412	17.15	40.69	38.81	23.32	9.754	0	4.66	1.02e+12
41	2.00	0.737	10.41	21.83	31.49	28.50	17.59	0	9.79	1.17e+12
42	1.79	0.282	5.335	14.58	22.06	15.15	3.131	0	8.24	1.37e+12
43	2.75	0.277	7.221	21.95	14.15	16.22	13.70	3	15.7	8.33e+12
44	2.03	1.038	29.37	43.28	34.96	28.66	7.363	2	13.4	4.74e+11
45	1.91	0.248	5.540	14.59	26.78	19.12	7.714	0	5.65	1.43e+12
46	1.81	0.551	16.28	28.14	17.47	10.42	6.205	0	4.42	1.72e+12
47	2.12	0.179	5.090	8.722	25.19	24.05	19.96	-99	-99	-99
48	2.35	0.386	9.840	30.80	33.42	44.45	28.70	0	11.8	4.28e+12
49	1.96	0.130	6.263	12.26	20.61	23.57	12.48	0	1.40	1.48e+12
50	2.92	0.296	9.159	25.80	40.72	28.25	21.91	0	8.62	3.72e+12
51	2.55	0.559	9.291	20.90	20.95	4.990	16.31	0	1.26	1.82e+12
52	1.94	0.208	6.285	11.61	19.85	18.14	7.037	0	2.37	1.72e+12
53	2.26	0.379	9.616	28.90	38.44	34.29	20.98	0	8.56	1.51e+12
54	1.88	0.704	4.882	29.71	30.02	36.79	7.011	0	0.672	1.41e+12
55	1.61	0.187	7.526	18.13	19.77	23.50	15.58	0	25.1	2.08e+12
56	1.61	0.284	7.408	19.38	21.56	17.52	9.390	0	2.67	1.00e+12
57	1.73	0.537	5.251	16.61	29.93	25.76	9.697	0	24.1	1.73e+12
58	2.77	0.165	7.150	14.23	13.25	8.367	8.701	2	20.9	2.33e+12
59	1.94	0.330	14.65	24.56	26.93	21.13	10.50	0	0.369	1.94e+12
60	1.27	0.433	10.52	27.31	44.89	44.77	34.52	0	9.25	7.57e+11

flag AGN is the contribution from an AGN to the host galaxy obtained from DecompIR: (0): only host galaxy, (1): % AGN $\leqslant$ 20%, (2): 20 < % AGN $\leqslant$ 40%, (3): 40 < % AGN $\leqslant$ 70%, (4): % AGN > 70%

Table 3 – *continued*

DOG ID	redshift	F_{24} (mJy)	F_{100} (mJy)	F_{160} (mJy)	F_{250} (mJy)	F_{350} (mJy)	F_{500} (mJy)	flag AGN	χ^2	L_{ir} ($L_\odot$)
61	2.00	0.745	15.31	25.86	38.35	47.96	29.10	0	50.1	3.18e+12
62	1.58	0.505	6.231	31.96	8.530	45.61	8.272	0	7.96	1.22e+12
63	1.88	0.621	17.10	39.68	41.01	29.16	21.66	0	6.60	6.77e+11
64	2.55	0.366	8.821	15.62	8.706	3.102	6.735	0	2.24	2.61e+12
65	1.76	0.419	9.343	19.55	28.59	27.63	20.37	-99	-99	-99
66	2.03	0.407	14.68	28.11	22.86	15.96	10.10	0	2.44	2.69e+12
67	2.85	0.497	16.95	27.73	10.42	8.087	11.99	0	14.7	4.00e+12
68	1.94	0.943	13.47	26.86	15.43	7.120	2.860	-99	-99	-99
69	1.62	0.925	43.88	66.54	54.21	32.34	6.816	-99	-99	-99
70	1.93	0.437	7.177	19.51	21.00	8.710	8.849	0	1.69	1.39e+12
71	2.53	0.132	16.52	44.25	51.89	34.34	23.83	3	1.20	2.98e+12
72	2.91	0.555	7.702	23.22	19.01	19.22	10.53	-99	-99	-99
73	1.61	0.395	13.92	23.40	31.45	13.30	11.82	4	1.44	2.49e+12
74	1.61	0.266	7.749	20.32	20.94	10.23	1.243	3	0.200	3.54e+11
75	2.70	0.256	6.372	13.61	29.14	24.31	23.73	0	1.67	3.36e+12
76	2.92	0.465	13.72	41.37	39.27	37.63	28.69	0	1.60	2.94e+12
77	2.00	1.487	10.00	17.00	29.15	27.47	5.519	0	14.1	1.48e+12
78	1.98	0.554	22.49	71.89	74.66	50.33	50.14	-99	-99	-99
79	2.11	0.359	14.87	21.01	25.52	18.83	15.39	0	11.0	2.55e+12
80	1.89	4.742	20.84	26.75	20.47	16.42	8.412	2	0.761	6.38e+11
81	2.33	1.385	30.01	59.63	62.33	50.04	24.83	0	3.97	1.31e+12
82	1.97	0.625	12.46	20.73	26.62	27.96	11.84	0	5.23	1.26e+12
83	1.98	1.059	28.67	36.87	32.63	40.06	27.67	3	15.6	2.07e+12
84	1.91	0.578	7.835	13.90	48.09	51.41	32.16	0	3.45	1.74e+12
85	2.58	1.917	14.49	18.95	13.09	9.595	2.781	0	15.9	2.26e+12
86	2.91	0.759	11.60	21.18	35.11	49.91	24.43	2	0.021	1.00e+12
87	2.34	0.637	7.290	17.49	20.34	23.81	13.98	0	6.19	2.14e+12
88	2.64	3.744	55.74	102.9	100.3	59.92	55.24	1	8.16	3.29e+12
89	2.20	0.860	12.87	22.32	12.75	19.16	21.22	0	19.6	5.25e+12
90	2.89	0.671	16.75	27.59	41.20	36.35	4.689	1	4.33	5.54e+11
91	2.88	0.931	5.011	11.63	15.30	13.39	16.10	1	5.19	8.52e+11
92	2.60	2.392	17.72	34.43	49.46	32.61	10.89	0	8.08	2.23e+12
93	1.73	3.131	8.783	10.84	18.91	13.82	2.563	0	12.8	1.76e+12
94	1.75	1.559	20.80	20.48	16.66	8.258	4.248	0	6.89	2.05e+12

Sanders D. B., Soifer B. T., Elias J. H., Neugebauer G.,
  Matthews K., 1988b, ApJl, 328, L35
Schinnerer E. et al., 2007, ApJs, 172, 46
Scoville N. et al., 2007, ApJs, 172, 38
Smolčić V. et al., 2014, MNRAS, 443, 2590
Taniguchi Y. et al., 2007, ApJs, 172, 9
Treister E. et al., 2009, ApJ, 706, 535
Weedman D. W., Le Floc'h E., Higdon S. J. U., Higdon
  J. L., Houck J. R., 2006, ApJ, 638, 613